Supplementary data

Alleviating trade-off between dark current and sensitivity of β-Ga_2O_3 X ray detector via defect engineering

Xinyu Liu, Yiyuan Liu, Yang Li, Zeliang Gao*, Kun Zhang, Wenxiang Mu*
State Key Laboratory of Crystal Materials, Institute of Novel Semiconductors, Institute of Crystal Materials, Shandong University, Jinan 250100, China

1. Supplementary experimental data

Crystal Growth

The crystal growth was conducted in a custom-designed edge-defined film-fed growth (EFG) method, equipped with a high-precision pulling and power control system. The pulling speed can be adjusted within 0–2000 mm/h, and the power system ranges from 0 to 30 kW with an accuracy of approximately 0.01 W. The EFG furnace relies on an induction coil for heating, with the crucible and mold fabricated from iridium. The crucible serves as the heating element for induction heating, and thermal insulation materials are placed between the heating element and the coil.

For β-Ga_2O_3 UID crystals, the raw material was β-Ga_2O_3 (99.999%) powder. For β-Ga_2O_3:Fe crystals, Fe_2O_3 (99.999%) powder was additionally added and mixed for 60 hours using a mixer. The mixed raw materials were heated to melting at a rate of 100–200 ℃/h. Capillary action caused the melt to rise through the slit and spread on the mold surface. After adjusting the power to an appropriate level, the system was stabilized for 2–3 hours. A high-quality seed crystal with [010] orientation was slowly lowered to contact the mold surface, and pulling began at 15–20 mm/h for the necking stage. After necking for 5–7 mm, the pulling speed and power were adjusted for the shouldering stage. When the crystal fully covered the mold surface, the shouldering was completed, and the body growth stage commenced. Upon growing to the expected length, the pulling speed was increased to detach the crystal, followed by slow cooling at 20–30 °C/h to conclude the growth process.

The β-Ga_2O_3 Annealed sample was obtained by heating β-Ga_2O_3 UID sample to 1200 °C in air atmosphere for 20 h, with a heating rate of 1.5 °C/min.

Device Fabrication

The as-grown single crystals were mechanically exfoliated along the (100) plane to obtain wafers with dimensions of 10×10×0.5 mm. Ti (20 nm) and Au (30 nm) electrodes were deposited on the devices via electron-beam evaporation. The electrode area of the detector is 1×1 mm^2.

Single-Crystal X-ray Diffraction (XRD)

XRD measurements of β-Ga_2O_3 single crystals were performed on a Bruker D8 diffractometer using Cu Kα radiation (λ = 1.54056 Å). The testing range was 10°–90° with a step size of 0.013°.

High-Resolution X-ray Diffraction (HRXRD)

HRXRD experiments were conducted using a Bruker D8 Discover system equipped with a four-crystal monochromator and parallel optical path system emitting Cu Kα1 radiation (λ = 1.54056 Å). The testing voltage and current were 40 kV and 40 mA, respectively, with a step size of 0.0005°/0.4 s.

Raman Spectroscopy

The Raman spectroscopy used in this study was a PHS-3C model manufactured by HORIBA, Japan. The experiment employed an excitation wavelength of 473 nm, conducted at room temperature with a wavenumber range of 50-1000cm^{-1}.

Fourier Transform Infrared Spectroscopy (FTIR)

FTIR measurements were performed on a Perkin Elmer Spectrum 100 spectrometer manufactured by PerkinElmer, USA, which can test wavelengths ranging from 1250 to 25000 nm with a scanning accuracy of 1 nm. The experimental testing range was 1500–8000 nm.

UV-Vis-NIR Spectroscopy

The ultraviolet-visible-near-infrared (UV-Vis-NIR) spectrometer used in this study is a Cary 7000 manufactured by Agilent, USA, with a wavelength testing range of 200–2500 nm and a scanning accuracy of 1 nm. The experimental testing range was 200–800 nm at a step size of 1 nm.

X-ray Photoelectron Spectroscopy (XPS)

XPS measurements were performed using a Thermo Fisher ESCALAB XI+ (Thermo Fisher Scientific). The C 1s peak was calibrated to 284.8 eV to correct for electrostatic effects in the recorded peaks.

X-ray Detector Performance Testing

A custom X-ray generation system was constructed to characterize the X-ray detection capability of β-Ga_2O_3 single crystals, with X-rays emitted from an X-ray tube (E7252X). Samples were placed in a shielded lead box to minimize environmental interference and human exposure. A Keithley 6517b high-precision electrometer was used to record current-voltage (I-V) and current-time (I-T) curves of β-Ga_2O_3 devices. During the experiment, detectors were exposed to a 40 keV tungsten anode X-ray tube. The X-ray dose rate was controlled by adjusting the tube current (10–25 mA). To obtain reliable X-ray detector metrics, a Piranha 655 X-ray multifunctional detector was used to calibrate the X-ray radiation dose, and the relationship between the dose rate and tube current of the X-ray equipment is shown in Supplementary Table S1. The X-ray radiation window measured 1×1.5 cm^2, with a distance of 70 cm between the window and the detector.

X-ray Imaging Testing

The X-ray imaging performance of β-Ga_2O_3 X-ray detectors was measured on a self-made displacement stage. The array detector for imaging was fabricated with Ti(20 nm)/Au(30 nm) pixel electrodes deposited on one side, while a full-area electrode was coated on the opposite side to cover the entire surface of the material. Each pixel was defined by a metal electrode with an area of 0.5×0.5 mm^2. The center-to-center distance between adjacent electrodes (pixel pitch) was 0.65 mm, resulting in an inter-electrode gap of 0.15 mm to ensure electrical isolation. During imaging, the object was placed between the planar-array detector and the X-ray source. The imaging was performed in a single-pixel scanning mode, where the photocurrent from each individual pixel was measured sequentially.[1-3]

2. Supplementary figures

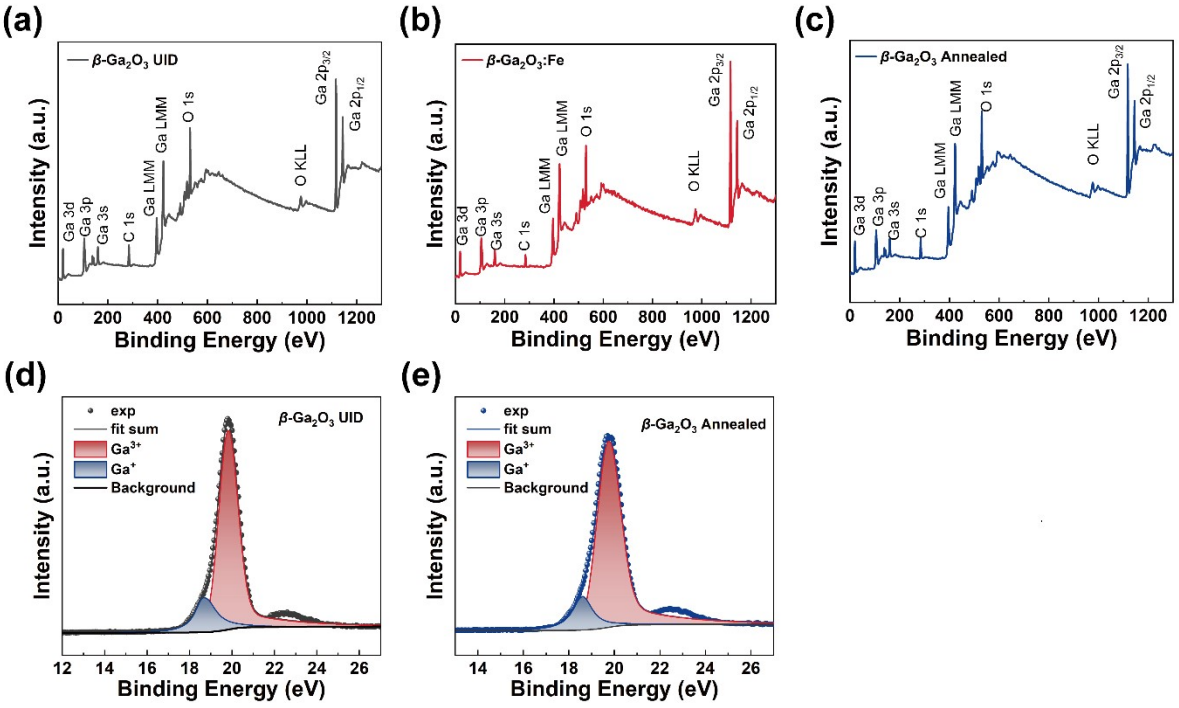

Figure S1. XPS spectra of (a) β-Ga_2O_3 UID, (b) β-Ga_2O_3:Fe, and (c) β-Ga_2O_3 Annealed. Ga 3d core-level spectra of (d) β-Ga_2O_3 UID and (e) β-Ga_2O_3 Annealed SCs.

Note:

Figure S1 displays the XPS survey spectra of different β-Ga_2O_3 single crystals. All β-Ga_2O_3 single crystals exhibit peaks corresponding to Ga 3d, Ga 3p, Ga 3s, C 1s, Ga LMM, O 1s, O KLL, Ga 2p3/2, and Ga 2p1/2. Notably, the XPS survey spectrum of the β-Ga_2O_3:Fe single crystal shows no appearance of Fe-related peaks, presumably due to the low doping concentration of Fe.

The Ga/O atomic ratio in β-Ga_2O_3 SCs was semi-quantitatively determined from the peak area ratio of Ga 3d to O 1s measured by X-ray photoelectron spectroscopy (XPS). The Ga/O ratios for the β-Ga_2O_3 UID and β-Ga_2O_3 Annealed samples are 0.75 and 0.69, respectively. It should be noted that due to the semi-quantitative nature of XPS, these results are for reference only.

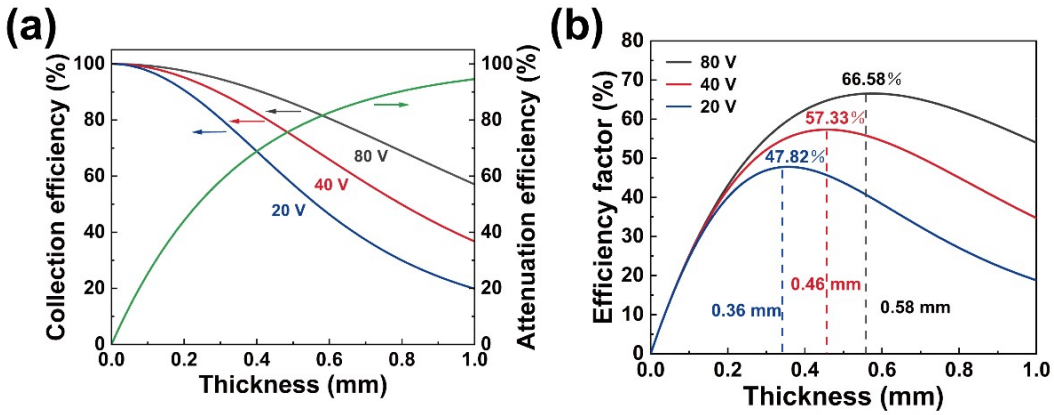

Figure S2. The dependence of (a) charge collection efficiency, (a) attenuation efficiency of 40 KeV X ray, and (b) efficiency factor on thickness

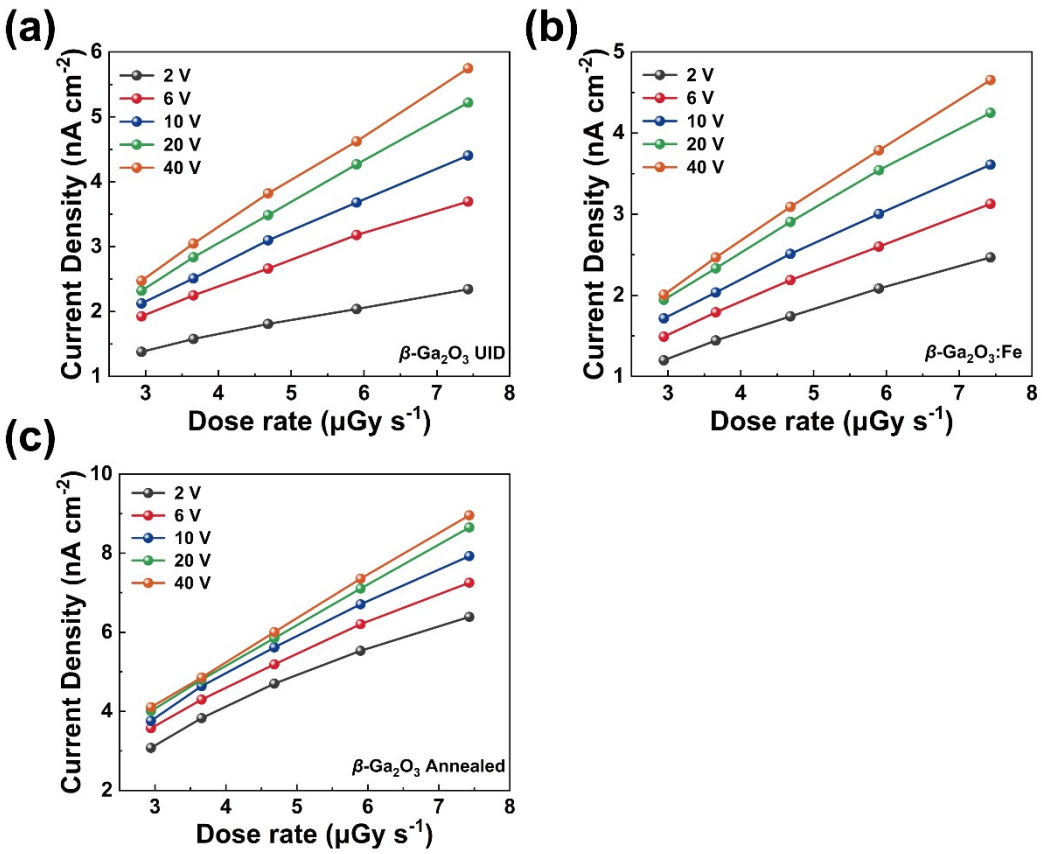

Figure S3. The dependence of net photocurrent density on dose rate for (a) β-Ga_2O_3 UID, (b)β-Ga_2O_3:Fe, and (c) β-Ga_2O_3 Annealed under different voltages.

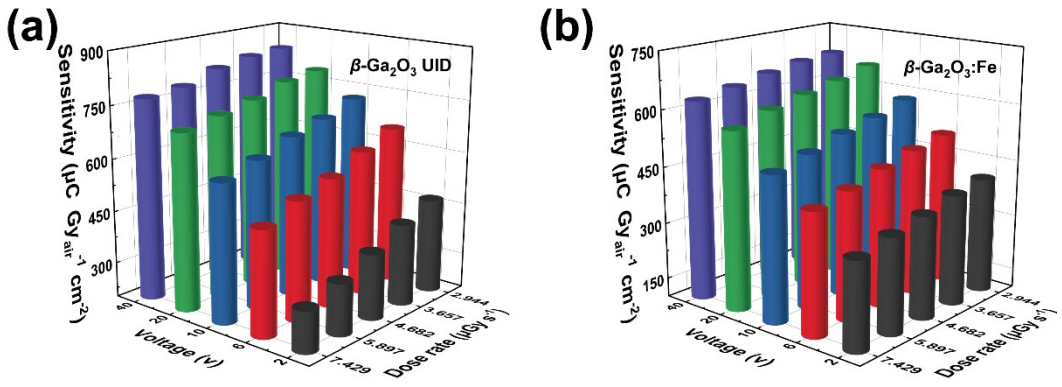

Figure S4. Sensitivity of (a) β-Ga_2O_3 UID, (b) β-Ga_2O_3:Fe X ray detector under different voltages and dose rates.

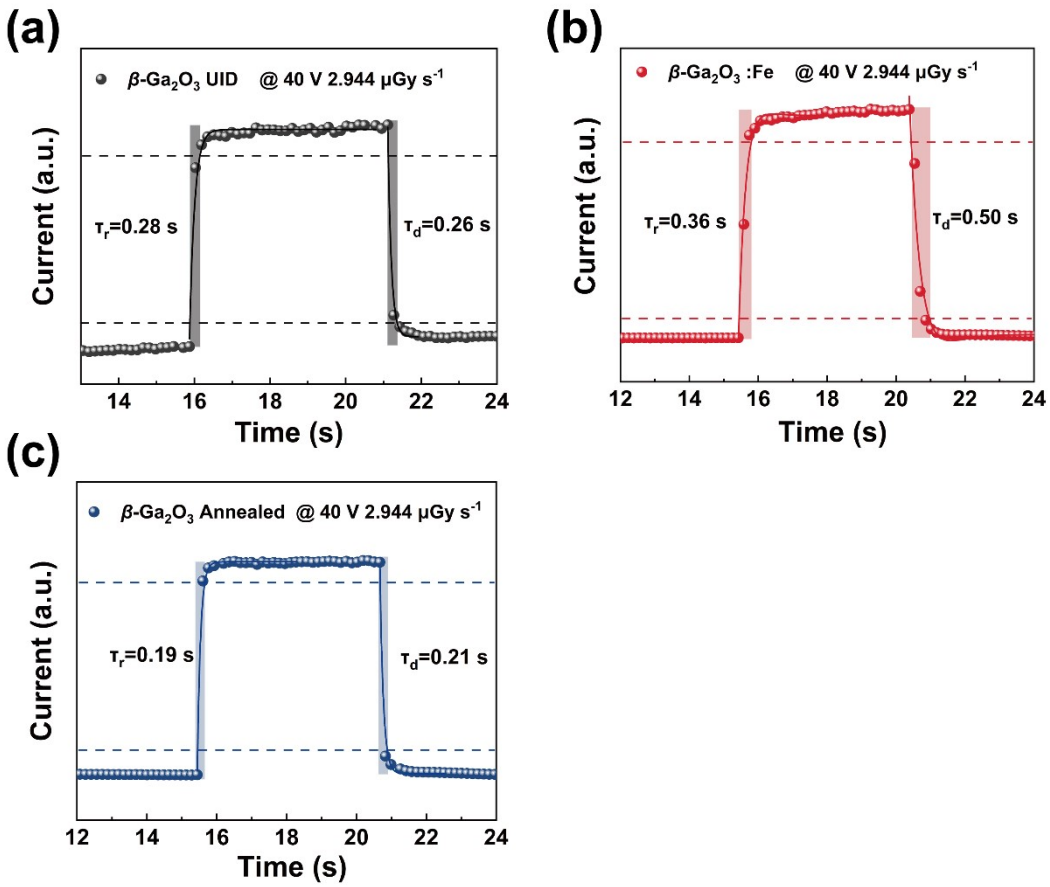

Figure S5. The response time of (a) β-Ga_2O_3 UID, (b) β-Ga_2O_3:Fe, and (c) β-Ga_2O_3 Annealed detectors.

Note: The experimental photocurrent vs. time data was first fitted with a standard exponential rise/decay function. The rise time (τ_r) and decay time (τ_d) were then calculated from the fitted curves as the time difference between the 10% and 90% points of the full signal swing.

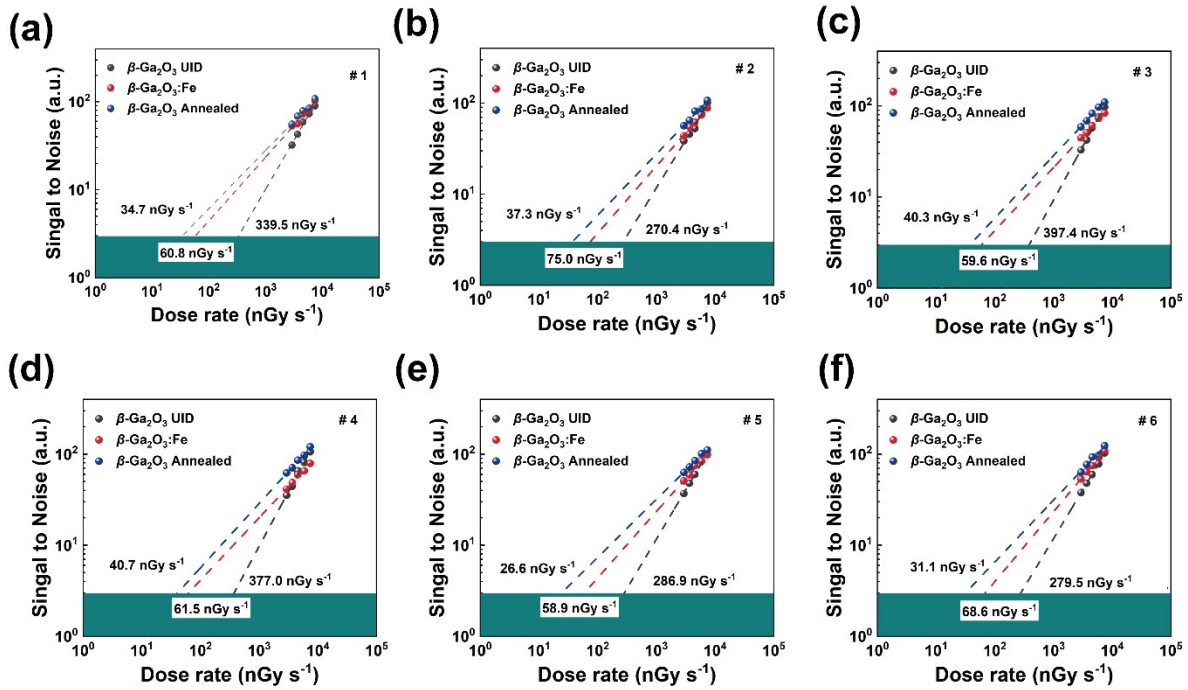

Figure S6. Linear fitting of dose rate versus signal-to-noise ratio for different β-Ga_2O_3 SC detectors.

Table S1. Dose rate calibration of 40 keV X-ray.

Tube current (mA)	**Dose rate (μGy s^{-1})**	**Corrected dose rate (μGy s^{-1})**
10	3.067	2.94432
12.5	3.809	3.65664
16	4.877	4.68192
20	6.143	5.89728
25	7.739	7.42944

Table S2 | Comparison of dark current, sensitivity and detection limit the β-Ga_2O_3 UID, β-Ga_2O_3:Fe, β-Ga_2O_3 Annealed detector with the reported detectors under different electric fields.

Material	**Tube Voltage (V)**	**X-ray Energy (KeV)**	**Voltage (V)**	**Dark current (nA)**	**Sensitivity ($\mu C\ Gy_{air}^{-1}\ cm^{-2}$)**	**Detection limit ($nGy\ s^{-1}$)**	**Ref.**
β-Ga_2O_3 Annealed (Bulk)	40	40	40	0.139	1394	34.7	This work
β-Ga_2O_3 UID (Bulk)	50	polychromatic	15	0.18(20v)	66	$\approx 6.95\times10^5$	4
β-Ga_2O_3:Mg (Bulk)	50	polychromatic	1000	0.28(200v)	338.9	$\approx 6.95\times10^4$	4
β-Ga_2O_3:Fe (Bulk)	50	polychromatic	1000	0.16(200v)	75.3	$< 8.31\times10^5$	5
β-Ga_2O_3:Al (Bulk)	50	polychromatic	350	0.12(200v)	851.6	$<9.8\times10^3$	6
Amorphous Ga_2O_3 (Film)	40	polychromatic	50	≈10	6.77	-	7
Nanocrystalline Ga_2O_3 (Film)	80	polychromatic	200	≈0.2	2.77	-	8
ε-Ga_2O_3 (Film)	30	polychromatic	20	≈4	19000	42300	9
ε-Ga_2O_3 (Film)	30	polychromatic	40	11	38	-	10
κ-Ga_2O_3 (Film)	40	polychromatic	500	0.0067	15.06	-	11
α-Ga_2O_3 (Film)	4.7-5.0	polychromatic	10	15.5	13.7	-	12
Amorphous Ga_2O_3 (Film)	20-40	polychromatic	15	-	952	11.23	13
β-Ga_2O_3/NiO (Film)	-	6 50	1.5	-	34000 8.7	42000	14
β-Ga_2O_3(Bulk+Film)	60	polychromatic	20	≈3000	1.2×10^5	-	15
β-Ga_2O_3 (Film)	60	polychromatic	50	-	1.23×10^5	-	16

Amorphous Se (Bulk)	20	20	2000	-	20	5500	[17]
$Cd_{0.1}Zn_{0.9}Te$ (Bulk)	-	-	-	-	318	5000	[18]
$Cs_2AgBiBr_6$ (Bulk)	50	polychromatic	50	-	105	59.7	[19]
$SnTe_3O_8$	120	120	1000	-	318	8.19	[1]
$Sn:Ga_2TeO_6$	40	40	800	≈0.007	575	97	[20]
$BaTeW_2O_9$	120	120	1000	-	404	21.9	[21]
$MAPbBr_3$	40	polychromatic	50	~1	10798	190	[22]

Note: The above performance comparison is provided for reference only, as the detectors were characterized under different X-ray energies (monochromatic or polychromatic spectrum) and with different electrode areas. It has been reported that both the X-ray energy and the electrode area have a significant impact on the device sensitivity.[9, 23]

References

1. X. Guo, Z. Gao, C. Li, J. Zhang and X. Tao, *Advanced Functional Materials*, 2023, **33**.
2. L. Liu, H. Zhou, J. Liu, X. Tian and Z. Gao, *Small*, 2025, **21**.
3. P. Zhang, Y. Hua, Y. Xu, Q. Sun, X. Li, F. Cui, L. Liu, Y. Bi, G. Zhang and X. Tao, *Advanced Materials*, 2022, **34**.
4. J. Chen, H. Tang, B. Liu, Z. Zhu, M. Gu, Z. Zhang, Q. Xu, J. Xu, L. Zhou, L. Chen and X. Ouyang, *ACS Applied Materials & Interfaces*, 2021, **13**, 2879-2886.
5. J. Chen, H. Tang, Z. Li, Z. Zhu, M. Gu, J. Xu, X. Ouyang and B. Liu, *Optics Express*, 2021, **29**, 23292-23299.
6. Z. Li, J. Chen, H. Tang, Z. Zhu, M. Gu, J. Xu, L. Chen, X. Ouyang and B. Liu, *ACS Applied Electronic Materials*, 2021, **3**, 4630-4639.
7. H. Liang, S. Cui, R. Su, P. Guan, Y. He, L. Yang, L. Chen, Y. Zhang, Z. Mei and X. Du, *ACS Photonics*, 2019, **6**, 351-359.
8. M. Chen, Z. Zhang, R. Zhan, J. She, S. Deng, N. Xu and J. Chen, *Applied Surface Science*, 2021, **554**, 149619.
9. Z. Zhang, Z. Chen, M. Chen, K. Wang, H. Chen, S. Deng, G. Wang and J. Chen, *Advanced Materials Technologies*, 2021, **6**.
10. J. Wang, L. Zhou, X. Lu, L. Chen, Z. Chen, X. Zou, G. Wang, B. Yang and X. Ouyang, *IEEE Photonics Technology Letters*, 2023, **35**, 89-92.
11. M. Girolami, M. Bosi, V. Serpente, M. Mastellone, L. Seravalli, S. Pettinato, S. Salvatori, D. M. M. Trucchi and R. Fornari, *Journal of Materials Chemistry C*, 2023, **11**, 3759-3769.
12. M. Kim, S. Kim, J.-H. Park, H. G. Cho, S. H. Gihm, D.-W. Jeon and W. S. Hwang, *Physica Status Solidi-Rapid Research Letters*, 2025, **19**.
13. Z. Wang, X. Wang, Y. Ma, J. Sun, S. Wang, Y. Jia, Y. He, X. Lu, D. Lin, Q. Zhu, Y. Shang, L. Liu, H. Chen and X. Ma, *Ieee Electron Device Letters*, 2024, **45**, 1879-1882.
14. Z. Zhang, M. Chen, R. Zhan, H. Chen, K. Wang, S. Deng and J. Chen, *Applied Surface Science*, 2022, **604**.
15. X. H. Hou, Y. Liu, S. Y. Bai, S. J. Yu, H. Huang, K. Yang, C. Li, Z. X. Peng, X. L. Zhao, X. Z. Zhou, G. W. Xu and S. B. Long, *Advanced Materials*, 2024, **36**.
16. Z. X. Peng, X. H. Hou, Z. Han, Z. Y. Gan, C. Li, F. H. Wu, S. Y. Bai, S. J. Yu, Y. Liu, K. Yang, X. Feng, H. Y. Zhan, X. L. Zhao, G. W. Xu and S. B. Long, *Advanced Functional Materials*, 2024, **34**.
17. S. O. Kasap, *Journal of Physics D-Applied Physics*, 2000, **33**, 2853-2865.
18. V. Dvoryankin, G. Dvoryankina, A. Kudryashov, A. Petrov, V. Golyshev and S. Bykova, *Technical Physics*, 2010, **55**, 306-308.
19. W. Pan, H. Wu, J. Luo, Z. Deng, C. Ge, C. Chen, X. Jiang, W.-J. Yin, G. Niu, L. Zhu, L. Yin, Y. Zhou, Q. Xie, X. Ke, M. Sui and J. Tang, *Nature Photonics*, 2017, **11**, 726-732.
20. Z. Liu, F. Guo, F. Hu, Y. Yin and Z. Gao, *Chemical Engineering Journal*, 2025, **518**.
21. F. Guo, F. Hu, Y. Song, L. Wang, Z. Gao and X. Tao, *Acs Applied Materials & Interfaces*, 2025, **17**, 9530-9538.

22. L. L. Gao, P. Fang, Y. Yang, P. Hu, S. Y. Yang, J. L. Zhu, F. Yang, H. Wang and K. Zhao, *Acs Applied Materials & Interfaces*, 2025, **17**, 65290-65299.
23. Y. Haruta, P. Huber, A. Hart, M. Bazalova-Carter and M. I. Saidaminov, *Acs Energy Letters*, 2023, **9**, 271-274.